View metadata, citation and similar papers at core.ac.uk
brought to you by CORE
provided by DSpace@MIT

Using Potassium Catalytic Gasification to Improve the Performance of Solid Oxide Direct Carbon Fuel Cells:

Experimental Characterization and Elementary Reaction Modeling

Xiankai Yu[a], Yixiang Shi[a,*], Hongjian Wang[a], Ningsheng Cai[a], Chen Li[b], and Ahmed F. Ghoniem[c]

[a] Key laboratory for Thermal Science and Power Engineering of Ministry of Education, Tsinghua University, Beijing 100084, China

[b] Huaneng Clean Energy Research Institute, Beijing 100098, China

[c] Center for Energy and Propulsion Research, Department of Mechanical Engineering, Massachusetts Institute of Technology, Cambridge, MA 02139, United States

Abstract

The performance of a solid oxide electrolyte direct carbon fuel cell (SO-DCFC) is limited by the slow carbon gasification kinetics at the typical operating temperatures of cell: 650-850^{o}C. To overcome such limitation, potassium salt is used as a catalyst to speed up the dry carbon gasification reactions, increasing the power density by five-fold at 700 - 850^{o}C. The cell performance is shown to be sensitive to the bed temperature, emphasizing the role of gasification rates and that of CO production. Given the finite bed size, the cell performance is time-dependent as the amount of CO available changes. A reduced elementary reaction mechanism for potassium-catalyzed carbon gasification was proposed using kinetic data obtained from the experimental measurements. A comprehensive model including the catalytic gasification reactions and CO electrochemistry is used to examine the impact of the catalytic carbon gasification process on the device performance. The power density is maximum around 50% of the OCV, where carbon utilization is also near maximum. Results show that bed height and porosity impact the power density; a thicker bed maintains the power almost constant for longer times while lower porosity delivers higher power density in the early stages.

* Corresponding author. Tel.: +86-10-62789955; Fax: +86-10-62770209.

Email: shyx@tsinghua.edu.cn.

Key words: catalytic gasification; direct carbon fuel cell; elementary reaction; modeling; heterogeneous chemistry

1. Introduction

Fuel cells, especially those operating directly on fossil fuels, constitute a promising technology for electricity generation because of their high efficiency and lower emission. Direct carbon fuel cells (DCFCs) have the added advantage of consuming an abundant and relatively cheap fuel that can be derived directly from coal, as well as their potential for enabling the separation of CO_2 from the products without extra equipment or energy penalty. DCFCs are classified according to the electrolyte, i.e., molten hydroxide [1, 3-6], molten carbonate [7-11] or solid oxide electrolyte [12-19], although combining molten carbonate and solid oxide electrolyte has also been suggested [20-22]. In this paper, we focus on solid oxide electrolyte DCFC (SO-DCFC). SOFCs operate at high temperature hence by improving the electrochemical reactivity as well as the ion diffusivity through the electrolyte, and do not suffer from liquid electrolyte consumption and corrosion. On the other hand, operating at high temperature can increase the thermal stresses and possible material degradation.

The anode reaction mechanism of the SO-DCFC is more complicated than in the gas-fueled counterpart. This mechanism has been investigated in several studies. Nakagawa and Ishida [12] placed charcoal in the fuel chamber of a solid oxide fuel cell, 5 mm away from the anode and used nitrogen as the anode gas carrier. They ran the cells at 1075, 1180 and 1275 K. Using the experimental results, they concluded that the electrochemical reactions were driven by the carbon monoxide produced via charcoal gasification according to the following reactions:

$$C + CO_2 \rightarrow 2CO \tag{1}$$

$$CO(Ni) + O^{2-}(YSZ) \rightarrow CO_2(Ni) + (YSZ) + 2e^- \tag{2}$$

$$\frac{1}{2}O_2 + 2e^- \rightarrow O^{2-} \tag{3}$$

Reaction 1, the Boudouard reaction, is the carbon gasification reaction responsible for production of CO, while Reaction 2 is the electrochemical oxidation reaction of CO,

which takes place at the anode triple phase boundary (TPB). Reaction 3 is the electrochemical reduction reaction at the cathode. Gür and Huggins [13] proposed an oxidation mechanism using an experiment in which they placed solid carbon adjacent to an yttria-stabilized-zirconia (YSZ) tube with platinum coated electrodes, and introduced helium as the anode gas. The temperatures of cell and carbon fuel were controlled independently.

In the experiments mentioned above, carbon can hardly be electrochemically oxidized directly (as in $C + 2O^{2-} \rightarrow CO_2 + 4e^-$ or $C + O^{2-} \rightarrow CO + 2e^-$), and therefore the anode reactions that determine the cell performance are reactions 1 and 2, together. In the absence of an external gasification medium such as CO_2, the products of the electrochemical reaction act as a gasification medium. Moreover, in a typical SO-DCFC, the temperature of the carbon fuel is the same as that of the cell, ranging from 600 to 1000^{o}C [14]. As reported in our previous work [23], reactions 1 and 2 strongly depend on temperature. The carbon gasification reaction is slow below 800^{o}C and hence it is likely to be the rate-limiting step determining the overall performance of DCFC.

It has been widely demonstrated that alkali metals are effective catalysts for carbon gasification [24-28]. Those metals have been used in coal gasification to raise its rate at lower temperatures. In a series of experiments, Lee and Kim [29] measured the catalytic activities of alkali and transition metal salts. Moulijn and Kapteijn [30] proposed a possible structure of the active intermediates for the K-catalysis and demonstrated the catalytic process pathways. Using molecular dynamics calculations, Chen and Yang [31] developed a unified mechanism for dry and wet carbon gasification by CO_2 and H_2O, respectively, using alkali metals as catalysts. They reported two kinds of oxygen intermediates/complexes dispersed in the alkali metal clusters, which could explain the observed phenomena that a catalyst changes the gasification rates without changing the activation energy. Struis et al. [32] and Huang et al. [33] suggested simplified models for catalytic carbon gasification processes and analyzing the kinetic behavior of metal catalyzed gasification.

There has been less effort to develop elementary reaction mechanisms for modeling carbon catalytic gasification, which is essential to better understand its role in improving the DCFC performance. In this paper, potassium was used to accelerate carbon

gasification . A series of experiments were conducted using potassium salt embedded in the carbon fuel, while fixing the temperature of the fuel cell to 750^{o}C and varying that of carbon fuel from 700 to 850^{o}C, in order to determine the impact of catalytic gasification on the DCFC performance. A comprehensive elementary reaction mechanism of carbon catalytic gasification was introduced based in part on the work in Refs. [31, 34, 39-41]. Kinetic data for the model were obtained by fitting the model to the experimental results. Combined with the SO-DCFC model proposed by our group [36-37], the performance of the cell was simulated to gain insight into the relative roles of gasification and electrochemistry, and to determine the impact of bed geometric design on the power density and carbon utilization.

The study reported in this paper utilizes a finite size carbon bed as the fuel, and examines the impact of the bed size on the power density and other cell performance characteristics as a function of time. As will be shown, given that the electrochemically active component here is CO, which is produced by the dry gasification of the carbon bed, and since the gasification rate depends on the bed geometry, the cell performance also time dependent. Moreover, conditions under which a steady performance can be achieved for a finite period of time are also explored.

In Section 2, we describe the experimental apparatus used to collect gasification kinetic and cell performance data. In Section 3, models for the gasification kinetics and the fuel cell performance are briefly described. Section 4 shows experimental and simulation results, as well as discussions regarding factors controlling cell performance. Conclusions are summarized in Section 5.

2. Experiment

2.1 Experimental setup

An anode-supported SOFC button cell fabricated by SICCAS (Shanghai Institute of Ceramics, Chinese Academy of Sciences) was used in this study. It consisted of a nickel/yttria-stabilized zirconia (Ni/YSZ) anode support layer (680μm), a nickel/scandia-stabilized zirconia (Ni/ScSZ) anode active interlayer (15μm), a ScSZ electrolyte layer

(20μm), and a lanthanum strontium manganite (LSM)/ScSZ cathode layer (15μm). The diameter of the cathode layer was 1.3cm and that of other layers was 2.6cm.

To examine the effect of catalytic gasification on the SO-DCFC performance, the carbon fuel and the button cell were separated to avoid possible carbon direct electrochemical oxidization. Figure 1 (a) and (b) show schematics of the test equipment. Located at the end of two coaxial alumina tubes, the button cell was supported by a horizontal alumina plate which was constrained by springs. The alumina plate with a hole in the middle on the anode side offered a channel for the anode fuel gases. A platinum (Pt) mesh was used as cathode current collector. The oxidant flowed into the inner tube to the cathode and passed through the porous Pt mesh. A Ni felt (thickness 2 mm) was fixed to the anode support layer with silver paste to collect the anodic current. The carrier/gasification gas was introduced into the carbon bed, which was contained in another alumina tube. For both the anode and cathode, Pt wires were used as voltage and current probes. The horizontal alumina plate had a through-hole of the same diameter as the cell cathode, and it was used to constrain the carbon bed. The layout of the carbon bed is exhibited in Figure 1 (a). The carbon fuel was placed in another small quartz tube under the button cell. A porous plate sintered of quartz sand was fixed to the quartz tube. The carbon fuel, quartz wool and corundum ceramic chips were placed on the plate sequentially. The anode gas flowed into the small quartz tube, through the porous plate, carbon fuel, quartz wool, alumina chips and finally to the button cell anode. The quartz wool and corundum ceramic chips were used to prevent the carbon fuel powder from being blown away by anode gas.

The device was enclosed in a quartz tube and heated by a furnace to the required temperature. Pure H_2 passed through the chamber for 1 h to fully reduce the anode at a flow rate of 50sccm (Standard Cubic Centimeter per Minute).

2.2 Catalyst addition and fuel preparation

Commercial carbon black (Black Pearls 2000, GP-3848, Cabot Corporation, USA), with 94.61% pure carbon, was used as a fuel, and it was crushed to a size of 150–200μm. Analytical reagent grade potassium carbonate was used as the catalyst precursor. The catalyst was added by impregnation, at a ratio of metal atom to carbon of 1:10 by weight.

The preparation of the carbon fuel and the K additive proceeded as follows: A sample of K_2CO_3 was stirred in de-ionized water. Next, an air-dried carbon black sample was added to the solution, stirred for 5 hours and kept for 24 hours. The sample was then dried at 70^{o}C for another 24 hours. After drying, the carbon black-potassium sample was crushed to a size of 150–200μm and stored in an air-tight plastic jar.

Figure 1. The SO-DCFC experimental setup. (a) The overall experimental setup used to test the performance of the DCFC, consisting of two part, the top part showing the fuel cell supported on an alumina plate and held by an outer tube, while an inner tube used to flow oxygen on the cathode side. The lower part shows the carbon bed and the gasification compartment. (b) Larger display of the fuel cell and current collectors.

2.3 Potassium catalytic carbon gasification experiment

The lower part of Figure 1 (a) describes the carbon gasification experimental setup. Before the experiment, 11.78mg fuel sample containing 10mg carbon black was loaded on the sintered quartz sand plate. After heating at a rate of 30^{o}C min^{-1} in an inert argon (Ar) atmosphere, the carbon bed was exposed to CO_2 at a flow rate of 200sccm while keeping its temperature at 725, 750, 775 and 800^{o}C. Gasification experiment was also conducted for pure carbon black (10 mg carbon black without catalyst) at 900^{o}C. The composition of the gaseous products sampled every 3 minutes was determined using Gas Chromatography (AutoSystem XL, PerkinElmer, USA). The total mass of the gases was obtained by integrating over the sample flow rate. The carbon conversion ratio Xc , that is the total consumption of solid carbon from the bulk fuel via gasification, is calculated using the following expression:

$$Xc = \frac{m_{CO}}{2m_0} \qquad [3]$$

where m_{CO} is the total mass of carbon within CO gas and m_0 stands for the overall carbon mass within the initial carbon fuel.

2.4 Fuel cell experiment

Figure 2 shows the standard procedure used in the fuel cell experiment. Before testing, the fuel sample is placed on the sintered quartz sand plate. The weight of the sample was 589mg containing 500mg pure carbon black. The temperature of the fuel cell was kept at 750^{o}C while the carbon bed was kept at a fixed temperature of 700, 750, 800 or 850^{o}C. In each case, a heating rate of 50^{o}C min^{-1} in an atmosphere of pure CO_2 was used. Next, 50sccm CO_2 was introduced into the carbon bed, and 100sccm of pure O_2 was introduced on the cathode side. After being reduced by pure H_2 at a flow rate of 50sccm, the fuel cell working voltage was kept at 0.7V throughout the testing process. Finally, the cell current density was measured by a four-probe method using an electrochemical workstation (IM6ex, Zahner--Elektric GmbH, Kronach, Germany).

Fig. 2 Standard procedure used in the fuel cell test experiment

3. Model development

3.1 Proposed potassium catalytic carbon gasification mechanism

The potassium catalytic carbon gasification mechanism proposed in this paper is reduced from mechanisms published in literature [31, 40-41]. The reaction parameters are shown in Table 1. The elementary reactions R.1 to R.5 are the gasification mechanism without a catalyst developed by Lee et al. [40-41]. The remaining elementary reactions involving the potassium catalyst are based on the unified mechanism of alkali catalytic gasification reactions of carbon proposed by Chen and Yang [31]. Kinetic data for the reactions without a catalyst are partly taken from [41]. The data for the catalytic reactions (R.6-R.8) in Table 1 were determined by matching the prediction to our experimental gasification data. In the gasification experiments, the conditions were chosen to resemble those in a thermogravimetric analysis (TGA) experiment, that is, the thickness of carbon bed was less than one millimeter and the inlet flow rate of CO_2 was as high as 40sccm. Therefore, the reactions were assumed to be kinetically–limited. The reaction rate constants not previously available for catalytic gasification were obtained by fitting the

model prediction to the experimental gasification data regarding carbon conversion at different fixed temperatures. Experimental and simulation results will be shown in the next Section, which discusses model calibration and validation.

The active intermediates: $[KO]$, $O[KO]$ and $O[KO](C)$ represent K_xO_y complexes or potassium clusters, oxygen complexes "dissolved" in potassium clusters, and the complexes of $O[KO]$ adsorbed on the active sites of carbon surface, respectively.

Table 1. Reduced potassium catalytic carbon gasification mechanism

3.2 SOFCs elementary reaction mechanism

The heterogeneous SOFCs elementary reactions mechanism shown in Table 2 is the same as that used in our previous papers [34-38]. Both the carbon gasification mechanism without a catalyst and the SOFCs electrochemistry mechanism have been experimentally validated before in similar experimental setups.

Model calculations were performed using the finite-element commercial software COMSOL MULTIPHYSICS®. The button cell performance was calculated at a given cell voltage (instead of a cell current). The average current density at the given voltage was derived from the local ionic current density in the electrolyte. For a detailed description of the gasification and SOFC membrane-electrode assembly (MEA) models, see Ref. [35-38]. In the gasification model, the species transport equations and momentum equation of the flow in a porous medium (using Darcy's law) were integrated throughout the carbon bed, while the source terms were evaluated using the applied gasification reactions mechanism. The SOFC MEA model consists of the species transport equations describing the flow through the porous electrodes, the charge balance equation (ion transport throughout all cell layers and electron transport through the two electrodes) described by Ohm's law, and the electrode electrochemistry described by the Butler-Volmer (BV) equation.

Table 2. The heterogeneous reaction mechanism on the Ni-based catalyst

4. Results and discussion

4.1 Model calibration and validation

The mechanistic model of the SO-DCFCs without a catalyst, based on the elementary kinetics for gasification and the MEA model for the fuel cell, was calibrated and validated in our previous work [37].

In order to verify the proposed potassium catalytic carbon gasification mechanism, gasification experiments described in Section 2.3 were conducted first. Figure 3 depicts the experimental results concerning carbon conversion via gasification.

Figure 3. Evolution of carbon conversion at 725, 750, 800^{o}C with a catalyst, and at 900^{o}C without a catalyst. The experimental results are shown in symbol, and those obtained using the reaction kinetics determined by fitting the mechanism listed in Table 1 are shown in lines.

The kinetics data obtained by fitting the experimental measurements to the mechanism shown in Table 1 predict the evolution of carbon conversion over the given temperature range with reasonable accuracy, showing that the proposed potassium catalytic carbon gasification mechanism is valid for our DCFC analysis. Furthermore, the conversion ratio at 900^{o}C without the K catalyst is even lower than that at 725^{o}C for the carbon bed infused with potassium salt, confirming that the catalytic effect of the potassium salt is capable of accelerating the carbon gasification. Correspondingly, it is possible to reduce the operating temperature of gasification to values consistent with those used for the fuel cell.

4.2 Performance of SO-DCFC with potassium catalytic carbon gasification

Figure 4 shows the power density of the SO-DCFC at 0.7 V, measured at different operating temperatures. Throughout the experiments, the temperature of the button cell

was kept at 750^{o}C and that of the fuel sample was controlled by the schedule described in Section 2.4. The figure shows the power density without and with a K-catalyst. The set temperature of the carbon bed is shown on top of the figure, and the measured value is shown by the corresponding staircase-like line. The power increases with the temperature of carbon bed because of the acceleration of the gasification reactions, but an observed drop is shown at higher temperatures, e.g., 800^{o}C, after a certain period of operation. A steeper drop is seen at 900^{o}C. This steep drop, as will be shown below, is due to the depletion of the fuel. In the case without a catalyst there is a much smaller rise in power at each step increase in temperature, followed by a very slow drop, again showing the acceleration of the non-catalytic reaction but also emphasizing the role of the catalyst.

Figure 4. The carbon bed temperature and power density of the SO-DCFC. The temperature of the cell was held constant at 750^{o}C, while those of the bed are shown by staircase plot. The upper triangular symbols show the experimental power density while using a potassium catalyst and the lower triangle for the experimental power density without a catalyst. The results of the simulation are shown for the power density and the bed temperature (solid lines).

Figure 5 exhibits the carbon conversion ratio and the gas composition immediately before the anode and above the carbon bed as shown in Figure 1 (a), both for CO and CO_2. As distinct from the gas fueled cell in which there is a steady supply of gaseous fuel, the solid fuel supply and hence the gaseous fuel supply to the anode in our DCFC is finite. The anodic gas composition and performance of the DCFC depend on the degree of carbon bed consumption, which increases during the gasification process. Therefore, given the finite solid fuel supply, the performance of the DCFC cannot be characterized simply by a simple polarization curve because of the process unsteadiness . The carbon conversion in the SO-DCFC system was evaluated as follows:

$$Xc = \frac{m_{CO} + \Delta m_{CO_2}^{elec}}{2m_0} \tag{4}$$

where m_{CO} is the total mass of carbon in the CO at the bed outlet, $\Delta m_{CO_2}^{elec}$ stands for the equivalent carbon content of CO_2 converted from CO by the electrochemical reaction. Here m_{CO} and $\Delta m_{CO_2}^{elec}$ are calculated by integrating the mass flow rate based on the bed outlet CO flow rate and the current with time. m_0 represents the initial overall mass within carbon fuel. As shown in the figure, Xc rises steadily indicating how much fuel is consumed, and the rise (first derivative of Xc) increases with temperature. Moreover, the gaseous fuel, CO, supplied to the anode increases stepwise as the temperature rises, consistent with the stepwise rise in the power density shown in Figure 4. Interestingly, the concentration of CO also shows a slow decrease after the stepwise rise, consistent with the power, and a steeper decrease at 800^{o}C and the steepest drop at 850^{o}C, when the fuel is almost all but depleted. At the anode inlet, while the CO mole fraction increases with increasing the temperature, CO_2, the product of the electrochemical reaction decreases, indicating that more of the fuel is used.

Figure 5. The carbon conversion and gas composition at the inlet to the anode. The solid inverted triangle and square symbols represent the experimentally measured mole fraction of CO_2 and CO, respectively, while the bold solid lines show the simulated results. Experimental and simulated carbon conversion values are shown by blank triangle and thin solid line, respectively.

Figure 4 and Figure 5 show good agreement between the modeling results and the experimental data. According to Figure 4, the power density produced by the SO-DCFC with potassium catalytic gasification is almost five times larger than that without a catalyst. Moreover, the performance of the catalyzed SO-DCFC starts to severely decline at the later stages because of the high carbon conversion demonstrated in Figure 5, which depletes the fuel. The opposite is true for the SO-DCFC without catalytic gasification, because of its slower fuel consumption. This suggests that potassium catalytic carbon

gasification accelerates the consumption of the carbon bed, which reduces the production of CO supply to the fuel cell anode at later times.

A sensitivity analysis to the carbon gasification reactions was conducted by comparing the relative change of the maximum power density when increasing and reducing the reaction rate by 20 percent. Figure 6 shows the modeling results, which indicate that the catalytic gasification reaction R6 $CO_2 + [KO] \overset{f}{\underset{r}{\rightleftharpoons}} CO + O[KO]$, is the key gasification reaction whose contribution far exceeds the other two non-catalytic reactions R1 $CO_2 + C_f \overset{f}{\underset{r}{\rightleftharpoons}} CO + O(C)$ and R2 $C_b + O(C) \longrightarrow CO + C_f$ [34]. Further analysis reveals that the rate of potassium salt catalyzed reaction R6 is two orders of magnitude faster than that of R1. However, the contribution of both of these reactions (R1 and R6) is theoretically the same from the perspective of gasification mechanism: functioning as the starting point of the gasification chain by producing the vital intermediates: namely the oxygen complexes and gaseous CO.

Fig. 6 Relative change of $P_{\max}$ obtained from the sensitivity analysis of the carbon gasification elementary reactions. Black blocks stands for result of increasing the reaction rate by 20%, and the white blocks corresponds to reducing the reaction rate by 20%. The relative change of $P_{\max}$ is expressed as: $(P_{\max} - P_0) / P_0$ where P_0 is the maximum power density without changing the elementary reaction rates artificially

The gas species distribution in the carbon bed and the fuel cell anode are shown in Figure 7. Results indicate that carbon conversion is much lower in the bed closer to the inlet even though the local CO_2 concentration there is higher. The reason is that fast consumption of CO by the fuel cell on the opposite side of the carbon bed accelerates the gasification reactions and shifts the Boudouard reaction toward producing more CO.

Figure 7. Distributions of the mole fractions of CO and CO_2 in the SO-DCFC system and carbon conversion in the carbon bed.

4.3 Effect of fuel cell voltages and carbon bed geometry

To examine the performance of the SO-DCFC system over a spectrum of operating conditions, simulations were performed at different operating voltages: 90%, 80%, 70%, 60% 50% and 40% of the OCV (the OCV is 0.916V based on using CO as a fuel), at 750^{o}C for both the carbon bed and fuel cell. Figure 8 shows the modeling results regarding the cell power density and carbon utilization.

Fig. 8 The power density P and carbon utilization η_{char} at different cell working voltages. Solid symbols show the power density, and open symbols show carbon utilization. In each case, the fuel cell works at a certain fixed voltage while the carbon bed is being consumed. The arrows point to the direction of decreasing operating voltage.

Here, carbon utilization is defined by the following expression:

$$\eta_{char} = \frac{\pi r_0^{\,2} j_{surf} / (4F)}{\int_H \frac{(1/2) R_{CO} m S_{gC}}{H} dx} \tag{4}$$

where r_o is the bed radius, i_{surf} the is current density, R_{CO} stands for the net production rate of CO in carbon bed, m is the mass of carbon bed, S_{gc} represents specific area of the carbon particle and H is the carbon bed height. The numerator in the expression stands for consumption rate of carbon by the electrochemical reaction $CO(Ni) + O^{2-}(YSZ) \xrightarrow{r} CO_2(Ni) + (YSZ) + 2e^-$, while the denominator is the total carbon consumption rate in the carbon bed. Specifically, according to the Boudouad

Reaction, the net rate of carbon consumption equals to half of the net production rate of CO, resulting in a net production rate of CO per unit bed height being $\frac{(1/2)R_{CO}\varepsilon_g\rho_g S_{gC}}{H}$. Therefore, the total net production rate of CO can be obtained by integrating $\frac{(1/2)R_{CO}\varepsilon_g\rho_g S_{gC}}{H}$ along the carbon bed height, and used as the denominator in the carbon utilization expression.

As expected, the fuel cell power density depends on the operating voltage, rising as the voltage decreases until it reaches a maximum (a characteristic of other SOFCs as well). Figure 8 indicates that the power density P is close to its maximum when the cell working voltage is lower than 50% of the OCV. Meanwhile, carbon utilization continuously increases as the cell voltage decreases, consistent with the rise in the power density, reaching close to 50% at its own maximum which occurs at voltage slightly below 50% of the OCV. Therefore, it may be concluded that operating the fuel cell at 50% of the OCV constitutes an optimal choice with respect to both high power density and carbon utilization. Overall, this is consistent with our previous conclusion for the case without using a gasification catalyst [34].

The SO-DCFC is modeled as a one-dimensional system, neglecting variations in radial direction, and hence the carbon bed height is an important carbon bed geometric characteristic that should impact the cell performance. Simulations were performed for different bed heights while keeping all other parameters constant. Figure 9 depicts the power density for different carbon bed heights, all at a fixed operating voltage of 50% of the OCV (the optimized value determined above) and temperature is 750^{o}C for both the carbon bed and fuel cell.

Fig. 9 The power densities P for different carbon bed heights at a fixed cell working voltage of 50% OCV (that is 0.458V).

It is clear that a thicker carbon bed improves the cell performance; not only the power density is higher, it is also more stable for a longer period of time. However, it

should be noted that the power output will drop beyond a certain bed height, and for the case considered here, a height of about 0.05m achieves maximum power at the early stages. Nevertheless, heights beyond 0.05m, maintain the power density almost constant for much longer periods of time since it helps keep the supply of CO steady. It is not clear why the power reaches a maximum at 0.05 m and why it first grows to a maximum and then gradually decreases.

Apart from the carbon bed height, the bed bulk porosity is another important geometric factor that should impact the power through the gasification rate and CO production. Figure 10 shows the relationship between power output and the initial carbon bed porosity. By changing the initial carbon bed bulk porosity while keeping the bed mass constant (and hence increasing its height) in the model, the power density variation with time is predicted and plotted.

Fig. 10 The power density P for different initial bulk porosities of the carbon bed at a fixed cell working voltage of 50% OCV (that is 0.458V). In all cases, the mass of the carbon bed is kept constant: 500mg pure carbon black and 89mg potassium salt, the same composition as experiments in Section 2.4.

It is apparent from the enlarged view that, at the early stages, the power density drops slightly while increasing the initial carbon bed bulk porosity. The impact of the bed porosity diminishes at longer times. This is interesting because, theoretically, higher porosity is expected to reduce the diffusion impedance, which should lead to better cell performance, but the opposite is observed. One reason is that higher porosity reduces the specific surface area available for the contact between gasification medium and carbon fuel. Since catalytically assisted gasification is mostly determined by reaction kinetics, this may turn out to be the dominant effect. At constant bed mass, higher porosity means larger carbon bed height, so the residence time increases with porosity or bed height. The competition of these effects leads to the slight decline in power density, at higher initial porosity.

5. Conclusion

In this paper we show experimentally that a potassium salt catalyst speeds up carbon gasification resulting in much higher power density when used in a SO-DCFC. In the experiments, the power density of SO-DCFC with potassium carbonate infused in the carbon bed is about five times higher than that without a catalyst. Therefore, adding such a catalyst is a promising alternative to lower the carbon gasification temperature so as to match the fuel cell temperature without degrading the performance. A reduced elementary reaction mechanism for potassium catalytic carbon gasification is proposed and its kinetic data are calibrated using experimental measurements. This makes it possible to build a set of elementary reactions library for SO-DCFC system involving catalytic carbon gasification processes.

While this work shows that, conceptually, using a gasification catalyst can improve the performance of a DCFC, future work should consider the thermal integration of the gasification process and the electrochemistry. While gasification reactions are endothermic, electrochemical oxidation reactions at these high temperatures are exothermic, and some of the heat generated by the latter can be used by the former. Extra heat may be required and that should be considered in the system design. Moreover, given the degradation observed in the cell performance as more carbon is consumed, continuous carbon feeding should also be considered.

Acknowledgements

This work was supported by the National Natural Science Foundation of China (20776078, 51106085) and the Seed Funding of Low Carbon Energy University Alliance. The first author acknowledges the great help of Professors Turgut M. Gür and Reginald E Mitchell and Mr. Greg Armstrong at Stanford. The authors also wish to acknowledge one of the reviewers for the thorough reading of the paper and the numerous thoughtful remarks and suggestions.

Nomenclature

References

[1] S. Zecevic, E.M. Patton, P. Parhami, Carbon, 42, 1983 (2004).

[2] S. Basu, Recent Trends in Fuel Cell Science and Technology, Anamaya, New Delhi, XI, 375 (2007).

[3] T.A. Edison, US, 460,122 (1891).

[4] W.W. Jacques, US, 555,511 (1896).

[5] G.A. Hackett, J.W. Zondlo, R. Svensson, J. Power Sources, 168, 111 (2007).

[6] T. Nunoura, K. Dowaki, C. Fushimi, S. Allen, E. Meszaros, M.J. Antal, Ind. Eng. Chem. Res., 46, 734 (2007).

[7] W.H.A. Peelen, M. Olivry, S.F. Au, J.D. Fehribach, K. Hemmes, J. Appl. Electrochem., 30, 1389 (2000).

[9] X. Li, Z. Zhu, J. Chen, R. de Marco, A. Dicks, J. Bradley, G. Lu, J. Power Sources, 186, 1 (2009).

[9] J.R. Selman, J. Power Sources, 160, 852 (2006).

[10] M. Steinberg, Int. J. Hydrogen Energy, 31, 405 (2006).

[11] J.F. Cooper, R. Krueger, N. Cherepy, US, 6815105 B2 (2004).

[12] N. Nakagawa, M. Ishida, Ind. Eng. Chem. Res., 27, 1181 (1988).

[13] T.M. Gür, R.A. Huggins, J. Electrochem. Soc., 139, L95 (1992).

[14] R. Liu, C. Zhao, J. Li, F. Zeng, S. Wang, T. Wen, Z. Wen, J. Power Sources, 195, 480 (2010).

[15] M. Ihara, S. Hasegawa, J. Electrochem. Soc., 153, A1544 (2006).

[16] S. Hasegawa, M. Ihara, J. Electrochem. Soc., 155, B58 (2008).

[17] H. Saito, S. Hasegawa, M. Ihara, J. Electrochem. Soc., 155, B443 (2008).

[18] M. Ihara, K. Matsuda, H. Sato, C. Yokoyama, Solid State Ionics, 175, 51 (2004).

[19] S. Li, A.C. Lee, R.E. Mitchell, T.M. Gur, Solid State Ionics, 179, 1549 (2008).

[20] S.L. Jain, Y. Nabae, B.J. Lakeman, K.D. Pointon, J.T.S. Irvine, Solid State Ionics, 179, 1417 (2008).

[21] K. Pointon, B. Lakeman, J. Irvine, J. Bradley, S. Jain, J. Power Sources, 162, 750 (2006).

[22] A.S. Lipilin, I.I. Balachov, L.H. Dubois, A. Sanjurjo, M.C. McKubre, S. Crouch Baker, M.D. Hornbostel, F.L. Tanzclla, US 2007/0269688 A1 (2007).

[23] C. Li, Y. Shi, N. Cai, International Conference on Power Engineering 2009 (ICOPE-09), Kobe, Japan, 2, 201 (2009).

[24] X. Li, C. Li, Fuel, 85, 1518 (2006).

[25] J. Yu, F. Tian, M.C. Chow, L.J. McKenzie, C. Li, Fuel, 85, 127 (2006).

[26] J. Wang, K. Sakanishi, I. Saito, Energy Fuels, 19, 2114 (2005).

[27] G. Domazetis, J. Liesegang, B.D. James, Fuel Process. Technol., 86, 463 (2005).

[28] Y. Ohtsuka, K. Asami, Catal. Today, 39, 111 (1997).

[29] W.J. Lee, S.D. Kim, Fuel, 74, 1387 (1995).

[30] J.A. Moulijn, F. Kapteijn, Carbon, 33, 1155 (1995).

[31] S.G. Chen, R.T. Yang, Energy & Fuels, 11, 421 (1997).

[32] R.P.W.J. Struis, C.V. Scala, S. Stucki, R. Prins, Chemical Engineering Science, 57, 3593 (2002).

[33] Y. Huang, X. Yin, C. Wu, C. Wang, Biotechnology Advances, 27, 568 (2009).

[34] X. Yu, Y. Shi, H. Wang, N. Cai, C. Li, R. I. Tomov, J. Hanna, B. A. Glowacki, A. F. Ghoniem, J. Power Sources 243 (2013) 159-171.

[35] Y. Shi, N. Cai, C. Li, C. Bao, E. Croiset, J. Qian, Q. Hu and S. Wang, J. Power Sources, 172, 235 (2007).

[36] C. Li, Y. Shi, N. Cai, J. Power Sources, 196, 754 (2011).

[37] C. Li, Y. Shi, N. Cai, J. Power Sources, 196, 5526 (2011).

[38] C. Li, Y. Shi, N. Cai, J. Power Sources, 195, 4660 (2010).

[39] J. D. Blackwood, A. J. Ingeme, J. Chem., 13, 194 (1960).

[40] L. Ma, Combustion and gasification of chars in oxygen and carbon dioxide at elevated pressure, Ph. D thesis, Stanford University, (2006).

[41] A. C. Lee, R. E. Mitchell, T. M. Gür, AIChE J., 55, 983 (2009).

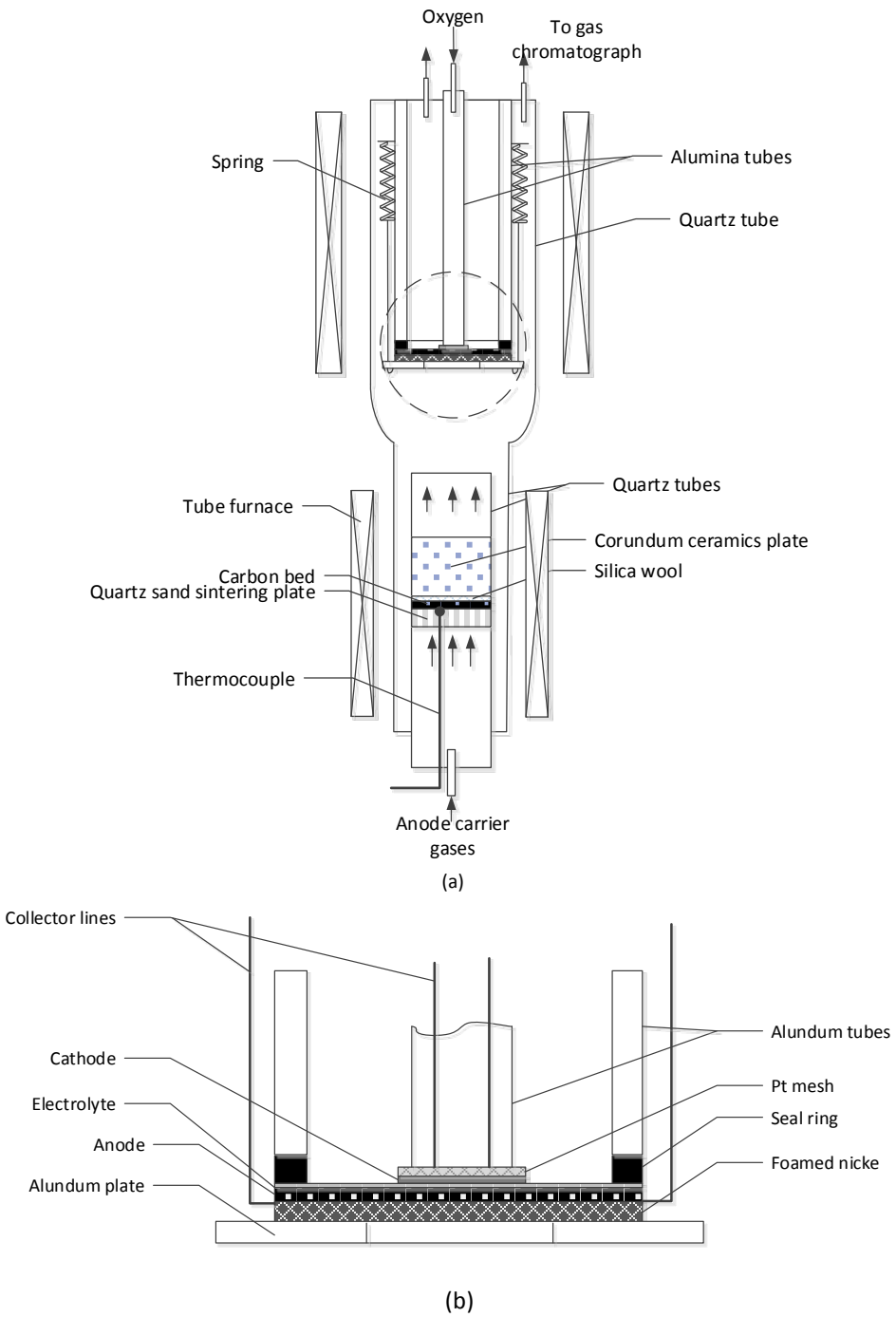

Figure 1. The SO-DCFC experimental setup. (a) The overall experimental setup used to test the performance of the DCFC, consisting of two part, the top part showing the fuel cell supported on an alumina plate and held by an outer tube, while an inner tube used to flow oxygen on the cathode side. The lower part shows the carbon bed and the gasification compartment. (b) Larger display of the fuel cell and current collectors.

Before testing

Place the carbon black and the button cell

↓

Feed H_2 (50sccm) to reduce the anode for one hour, keep the cell at 750^oC, and the carbon black at $\leq$ 200^oC

Discharge at 0.7V: electrochemical measurements and anodic gas analysis

Anode: H_2 at 50sccm; cathode: O_2 at 100sccm; cell at 750^oC; carbon black at $\leq$ 200^oC

↓

Anode: CO_2 at 50sccm; cathode: O_2 at 100sccm; cell at 750^oC; carbon black at $\leq$ 200^oC

↓

Anode: CO_2 at 50sccm; cathode: O_2 at 100sccm; cell at 750^oC; carbon black at 700, 750, 800 and 850^oC

Fig. 2 Standard procedure used in the fuel cell test experiment

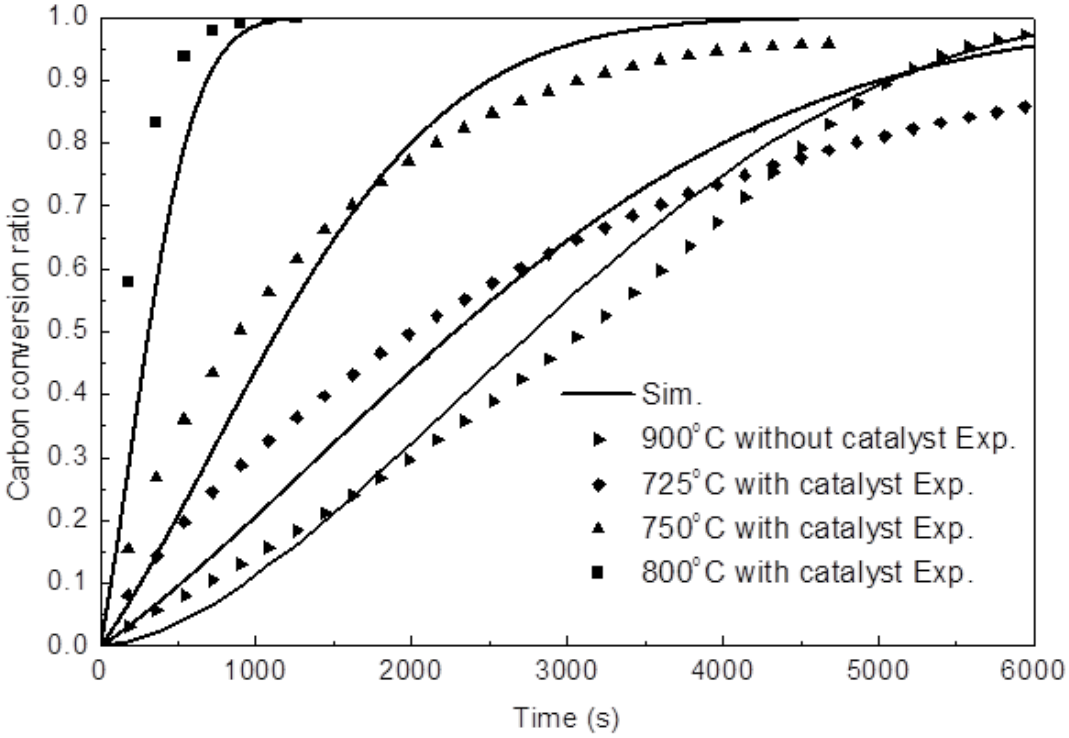

Figure 3. Evolution of carbon conversion at 725, 750, 800°C with a catalyst, and at 900°C without a catalyst. The experimental results are shown in symbol, and those obtained using the reaction kinetics determined by fitting the mechanism listed in Table 1 are shown in lines.

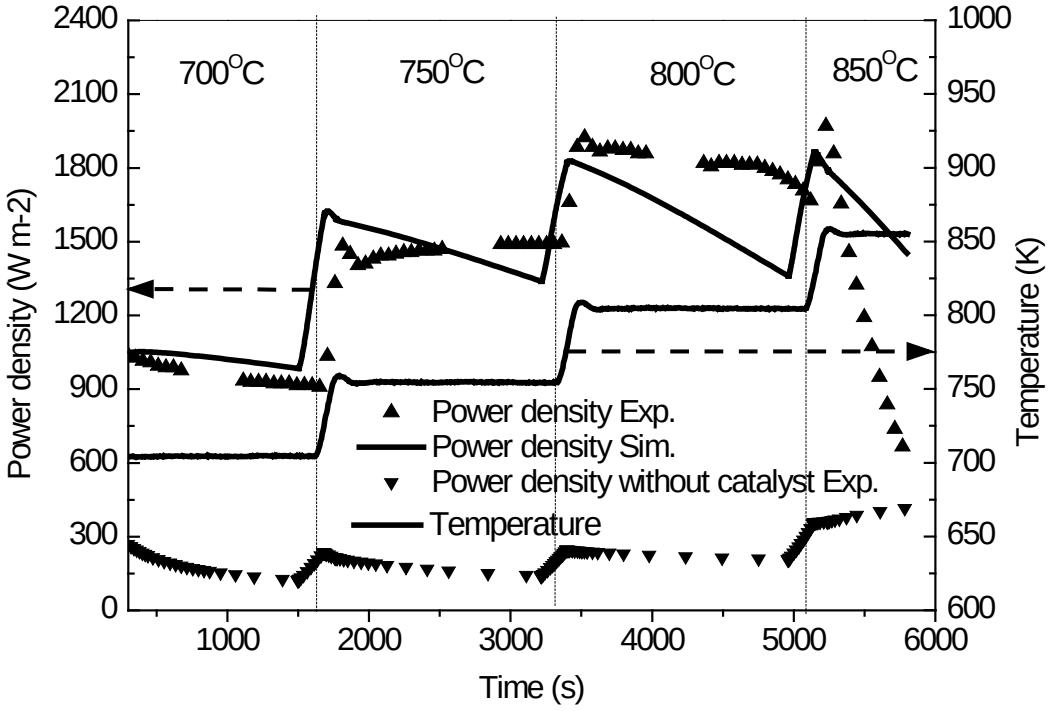

Figure 4. Carbon bed temperature and power density of the SO-DCFC. The temperature of the cell was held constant at 750°C, while that of the bed are shown by the staircase. The upper triangular symbols show the experimental power density while using a potassium catalyst and the lower triangular for the experimental power density without a catalyst. The results of the simulation are shown for power density and bed temperature (solid lines).

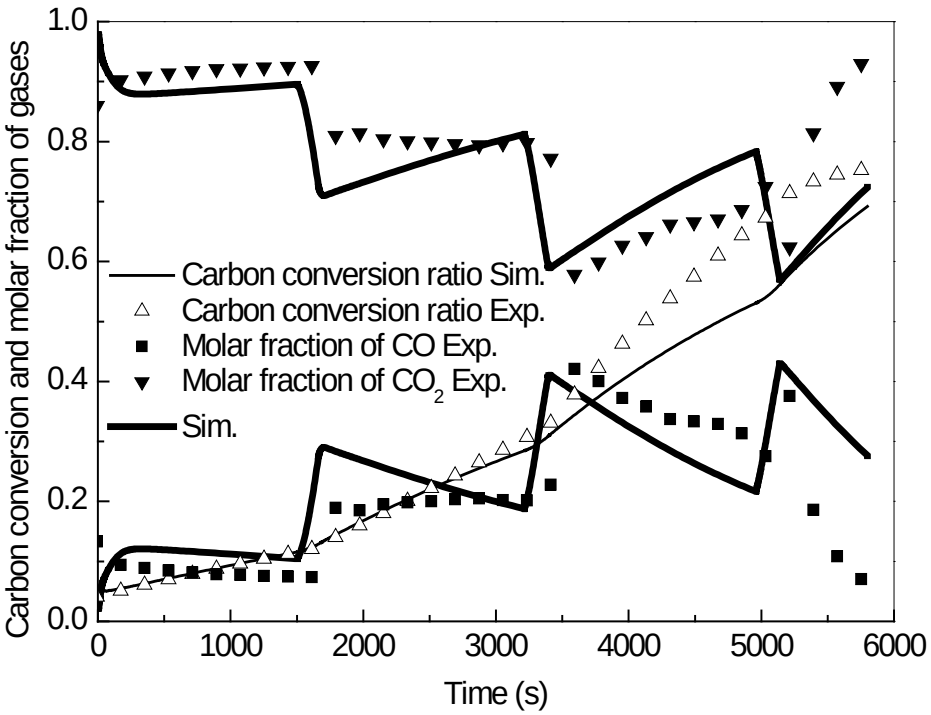

Figure 5. The carbon conversion and gaseous compositions at the inlet to the anode. The solid symbols of lower triangular and square stand for experimental fraction of CO_2 and CO, while the bold solid lines show the simulating results. Experimental and simulating values of carbon conversion are shown by blank upper triangular and thin solid line.

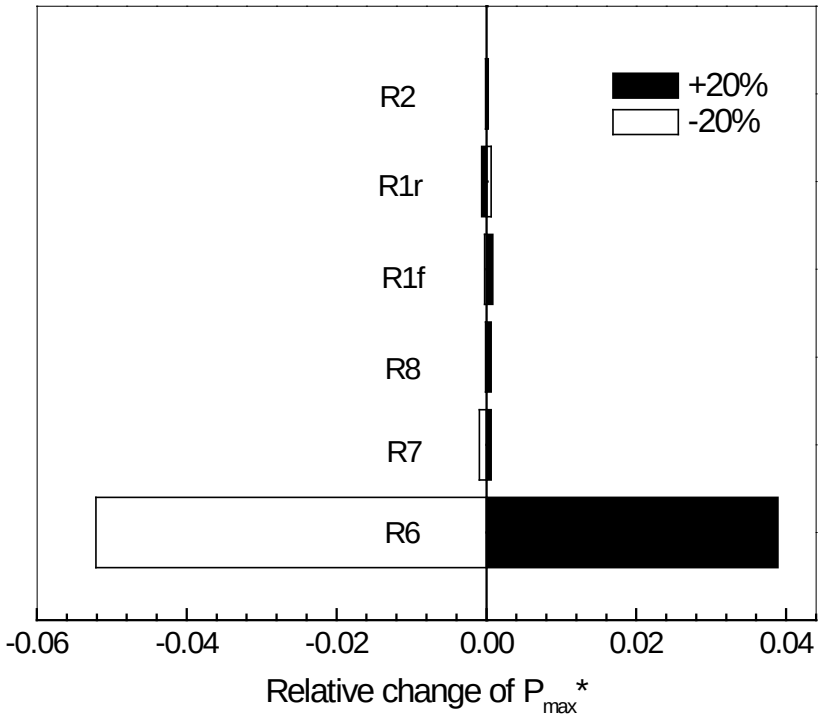

Fig. 6 Relative change of P_{max} obtained from the sensitivity analysis of the carbon gasification elementary reactions. Black blocks stands for the simulation results increasing the reaction rate by 20% and white blocks corresponds to reducing reaction rate by 20%. The relative change of P_{max} is expressed as: $(P_{max} - P_0) / P_0$ where P_0 is the maximum power density without changing the elementary reaction rates artificially

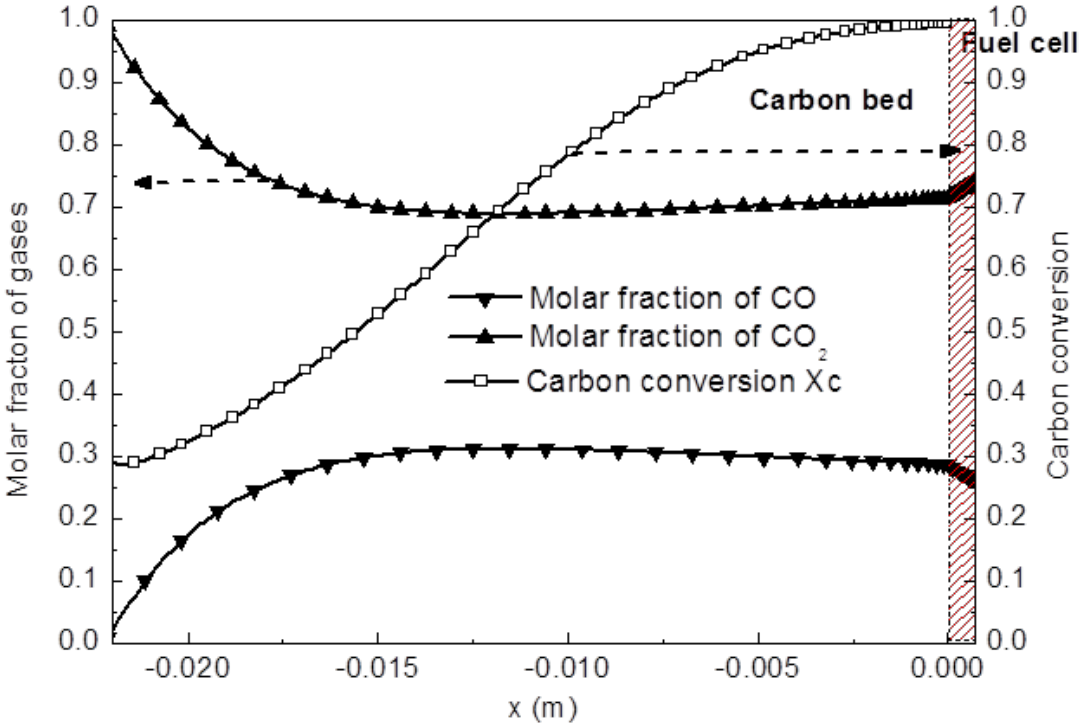

Figure 7. Distributions of molar fractions of CO and CO_2 in SO-DCFC system and carbon conversion in carbon bed.

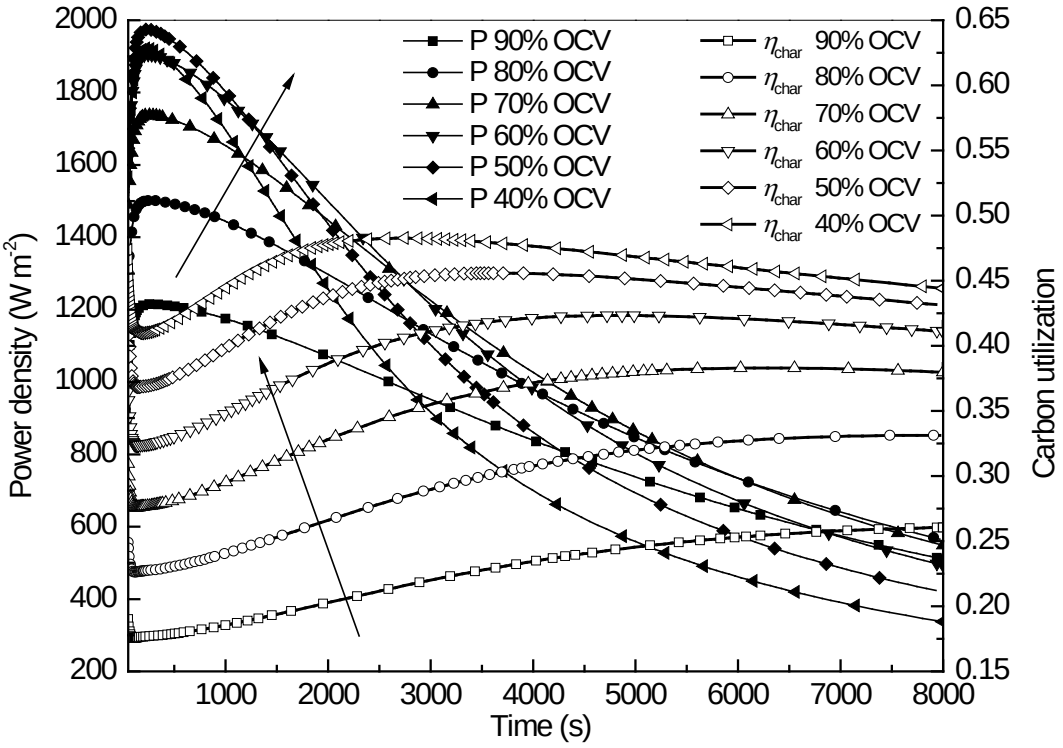

Fig. 8 The power density P and carbon utilization η_{char} at different cell working voltages. Solid symbols show the power, and open symbols show carbon utilization. In each case, the cell voltage is maintained at the same value while the carbon bed is being consumed. The arrows point to the direction of decreasing the operating voltage.

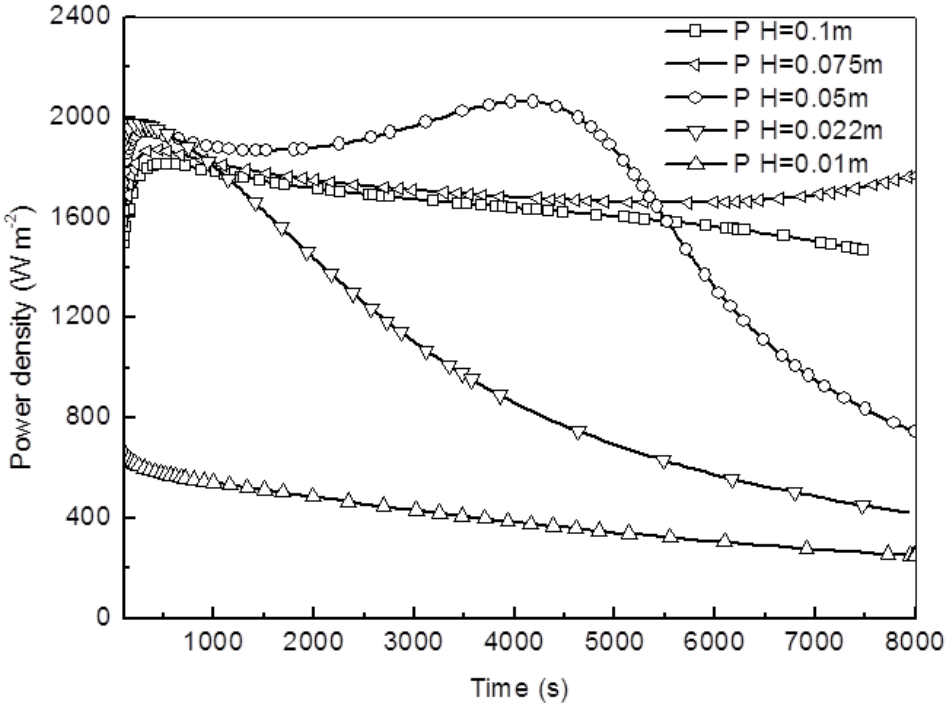

Fig. 9 The power densities P for different carbon bed heights at a fixed cell working voltage of 50% OCV (that is 0.458V).

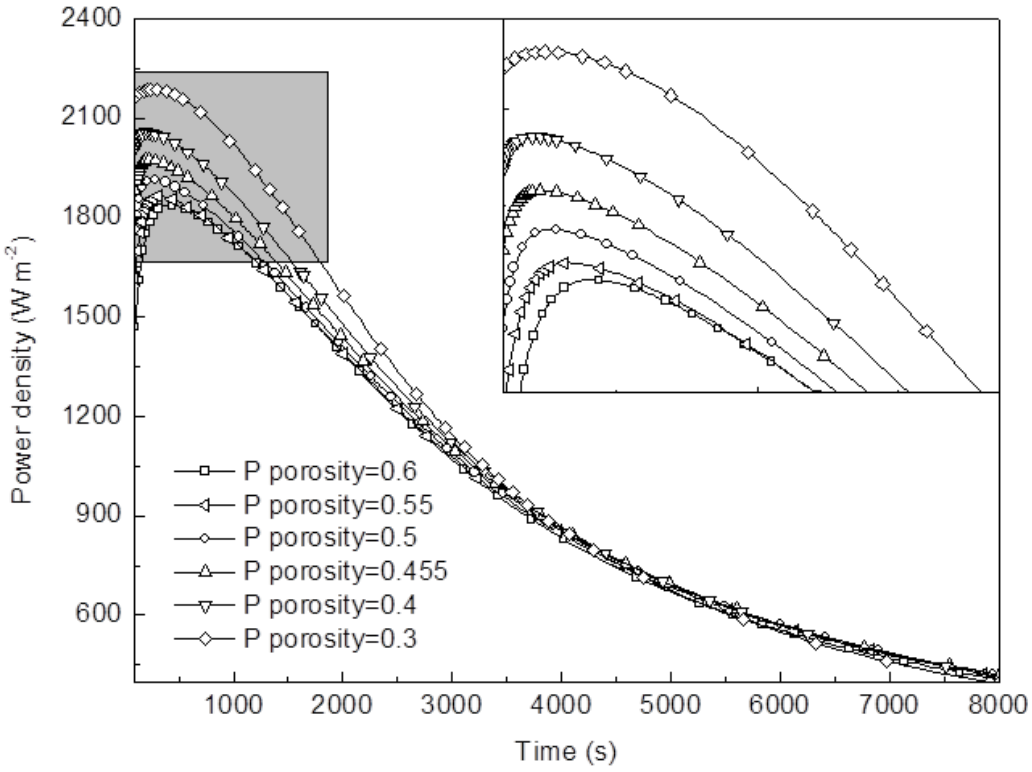

Fig. 10 The power density P for different initial bulk porosities of the carbon bed at a fixed cell working voltage of 50% OCV (that is 0.458V). In all cases, the mass of the carbon bed is kept constant: 500mg pure black carbon and 89mg potassium salt, the same composition as experiments in Section 2.4.

Nomenclature

A pre-exponential factor (in terms of cm, mol and s)

C_b bulk carbon atom

C_f free carbon site

$O(C)$ adsorbed oxygen atom species on carbon site

$CO(C)$ adsorbed carbon monoxide species on carbon site

$[KO]$ the K_xO_y complex or the potassium cluster

$O[KO]$ the oxygen complex "dissolved" in the potassium cluster

$O[KO](C)$ the complex of $O[KO]$ adsorbed on the active sites of the carbon surface

E activation energy (kJ mol^{-1})

H height of carbon bed (m)

k reaction rate constant (in terms of m, mol and s)

m total mass of carbon bed (kg)

m_0 total mass within initial carbon fuel (kg)

m_{CO} total mass of carbon in CO at the bed outlet (kg)

$\Delta m_{CO_2}^{elec}$ equivalent total carbon content of CO_2 converted from CO by electrochemical reaction (kg)

S_{gc} specific area of carbon particle (m^2 kg^{-1})

TPB three-phase boundary

x coordinate of x axis (m)

X_c carbon conversion ratio

OCV open circuit voltage (V)

ref reference

η_{char} carbon utilization degree

Table 1. Reduced Potassium Catalytic Carbon Gasification Mechanism

		A[a]	σ[b] (KJ mo^{-1})	E[a] (kJ mol^{-1})
Elementary Reactions Without Catalyst				
R.1f	$CO_2 + C_f \underset{r}{\overset{f}{\rightleftharpoons}} CO + O(C)$	5e-3	--	185
R.1r		108	--	89.7
R.2	$C_b + O(C) \longrightarrow CO + C_f$	1e13	28	375
R.3	$C_b + CO_2 + O(C) \longrightarrow 2CO + O(C)$	1e-4	--	58
R.4f	$C_f + CO \underset{r}{\overset{f}{\rightleftharpoons}} CO(C)$	0.89	--	148
R.4r		1e13	53	455
R.5	$CO + CO(C) \longrightarrow CO_2 + 2C_f$	1.01e7	--	262
Potassium Catalytic Elementary Reactions				
R.6f	$CO_2 + [KO] \underset{r}{\overset{f}{\rightleftharpoons}} CO + O[KO]$	7.572	--	245
R.6r			--	
R.7f	$C_f + O[KO] \underset{r}{\overset{f}{\rightleftharpoons}} O[KO](C)$	9.15e12	--	190.3
R.7r			--	
R.8	$C_b + O[KO](C) \longrightarrow CO + C_f + [KO]$	9.58e15	--	287.8

[a] Arrhenius parameters for the rate constants are written in the form: $k = A \bullet \exp(-E/RT)$

[b] For k_2 and k_{4r}, the activation energy is fitted to the normal distribution because the activation energy for species in the two reactions is not the same all through the carbon surface sites:

$$k = \int_0^{+\infty} A\exp(-\frac{E}{RT}) \bullet \frac{1}{\sqrt{2\pi}\sigma} \exp(-\frac{(E-E_a)^2}{2\sigma^2}) dE$$

Table 2. The heterogeneous reaction mechanism on the Ni-based catalyst

		A^c (cm, mol, s)	n^c	E^c (kJ mol^{-1})
Adsorption And Desorption Reactions				
RR.1f	$O_2 + Ni(s) + Ni(s) \underset{r}{\overset{f}{\rightleftharpoons}} O(s) + O(s)$	1e-2	--	0
RR.1r		4.283e23	--	474.95
RR.2f	$CO_2 + Ni(s) \underset{r}{\overset{f}{\rightleftharpoons}} CO_2(s)$	1e-5	--	0
RR.2r		6.447e7	--	25.98
RR.3f	$CO + Ni(s) \underset{r}{\overset{f}{\rightleftharpoons}} CO(s)$	5e-1	--	0
RR.3r		3.563e11	--	111.27
		$\theta_{CO(s)}$ [d]		-50.0
Surface Reactions				
RR.4f	$C(s) + O(s) \underset{r}{\overset{f}{\rightleftharpoons}} CO(s) + Ni(s)$	5.2e23	--	148.10
RR.4r		1.354e22	-3	116.12
		$\theta_{CO(s)}$ [d]		-50.0
RR.5f	$CO(s) + O(s) \underset{r}{\overset{f}{\rightleftharpoons}} CO_2(s) + Ni(s)$	2e19	--	123.6
		$\theta_{CO(s)}$ [d]		-50.0
RR.5r		4.563e23	-1	89.32
Transport of Bulk Oxygen Species				
RR.6f	$O^{2-}(YSZ) + (YSZ, bulk) \underset{r}{\overset{f}{\rightleftharpoons}} O^{2-}(YSZ, bulk) + (YSZ)$			
RR.6r				
Anode Electrochemistry				
RR.7f	$CO(Ni) + O^{2-}(YSZ) \underset{r}{\overset{f}{\rightleftharpoons}} CO_2(Ni) + (YSZ) + 2e^-$			
RR.7r				

[c] Arrhenius parameters for the rate constants are written in the form: $k = AT^n \exp(-E / RT)$

[d] Coverage-dependent activation energy